

PV-SSD: A Projection and Voxel-based Double Branch Single-Stage 3D Object Detector

Yongxin Shao, Aihong Tan, Zhetao Sun, Enhui Zheng

Abstract—LIDAR-based 3D object detection and classification is crucial for autonomous driving. However, inference in real-time from extremely sparse 3D data poses a formidable challenge. To address this issue, a common approach is to project point clouds onto a bird’s-eye or perspective view, effectively converting them into an image-like data format. However, this excessive compression of point cloud data often leads to the loss of information. This paper proposes a 3D object detector based on voxel and projection double branch feature extraction (PV-SSD) to address the problem of information loss. We add voxel features input containing rich local semantic information, which is fully fused with the projected features in the feature extraction stage to reduce the local information loss caused by projection. A good performance is achieved compared to the previous work. In addition, this paper makes the following contributions: 1) a voxel feature extraction method with variable receptive fields is proposed; 2) a feature point sampling method by weight sampling is used to filter out the feature points that are more conducive to the detection task; 3) the MSSFA module is proposed based on the SSFA module. To verify the effectiveness of our method, we designed comparison experiments. We tested them on the test set of the KITTI dataset on ‘Car’ class and ‘Cyclist’ class (3D AP of 86.71, 78.53, 74.09 for ‘Car’ class on Easy, Mod., Hard; 3D AP of 78.84, 63.00, 55.85 for ‘Cyclist’ class on Easy, Mod., Hard).

Index Terms—Point cloud, 3D object detection, LIDAR.

I. INTRODUCTION

AT this stage, AI-related technologies are constantly developing, and various applications are emerging. As an important part of the perception layer of autonomous driving, efficient object detection methods can provide a solid foundation for behavioral decisions in autonomous driving. Object detection methods need to detect moving objects such as cars, pedestrians, and cyclists in the current environment in real time and accurately detect their location and orientation. Although significant progress has been made in image-based 2D object detection [1]–[9] at this stage, compared with 3D space, 2D space lacks depth information. It cannot accurately describe the position and orientation of objects. The subsequently proposed depth camera-based [10]–[13] and multi-view image-based 3D object detection methods [14]–[17] make up for the lack of depth information from 2D cameras. Still, the cameras are sensitive to the light environment and often perform poorly in complex urban environments. Compared to images, LIDAR enables easier description of object poses in

Yongxin Shao, Aihong Tan, Zhetao Sun, Enhui Zheng and Tianhong Yan are with the School of Mechanical and Electrical Engineering, China Jiliang University, Hangzhou, 310018, China. (email: syx1536505936@163.com; Tanah@cjlu.edu.cn; zhetaosun@163.com; enhuizheng@cjlu.edu.cn; thyan@163.com). Aihong Tan is the Corresponding Author.

3D space. Unlike images, point clouds have separate objects without occlusion, thereby eliminating the occlusion problem. Additionally, LIDAR is more robust to illumination changes [18]–[22].

However, there are some challenges in point cloud-based 3D object detection methods. For example, (1) sparsity; (2) disorder; and (3) rotation invariance [20]. These properties of point clouds lead to the fact that it is impossible to perform feature extraction directly with 2D convolution, as images do. A common approach is to convert point clouds into data representations that resemble images by projecting them onto, for example, bird’s-eye or perspective view. Feature extraction is then carried out using 2D convolutional neural networks [23]–[29]. However, this image-like data representation can result in significant loss of feature information from the point clouds. This is especially true for objects with few reflective points, such as cyclists, where information loss can significantly impact subsequent detection tasks. In addition, although detection under the bird’s-eye view can avoid occlusion, the point cloud data under the bird’s-eye view is sparse and contains less semantic information. AVOD, MV3D, and H23D R-CNN [25]–[27] address this issue by either increasing the image input or adding a perspective view of the point cloud. Compared to the perspective view of the point cloud and image, there is no natural occlusion for object separation in the bird’s-eye view. On the other hand, the perspective view of point clouds images and images contains rich semantic information compared to the bird’s-eye view of the point cloud. By complementing these two approaches, it can greatly improve the aforementioned problem. However, this paper proposes a different approach to compensate for the lack of bird’s eye view features by increasing the input of voxels containing local point cloud semantic features.

In the backbone network, as the network deepens, the resolution of the feature map of projected features will decrease, while the perceptual field of voxel features remains unchanged. This leads to differences in the resolution and perceptual range between the projected and voxel features, which poses challenges to subsequent feature fusion. To address this issue, we propose the Variable Receptor Field Voxel Feature Extraction layer (VR-VFE layer) that ensures the voxel perceptual range and resolution are the same as the projected features within each stage. The VR-VFE module preserves rich semantic features of voxel features as the network depth increases. Additionally, we introduce a feature sampling method called the Re-Voxelization Layer, which filters out useful feature points from a limited number based on feature point weights. Within VR-VFE, we design Point-wise Feature Weighting

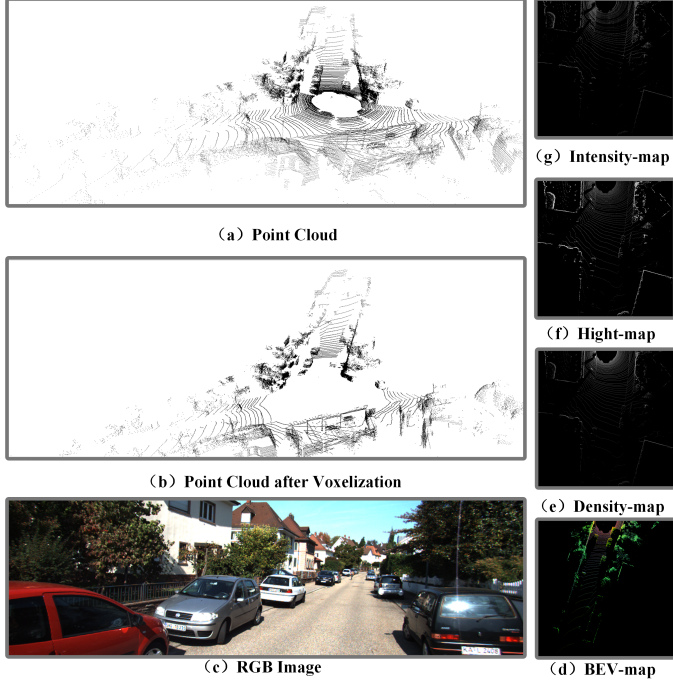


Fig. 1. An illustration of (a) Point Cloud, (b) Point Cloud after voxelization, (c) RGB Image, (d) BEV-map, (e) Density-map, (f) Height-map, and (g) Intensity-map. Each voxel in (b) contains 12 points, and the size of the voxel is [0.1m, 0.1m, 0.125m]. Density-map, Height-map, and Intensity-map are the three channels of BEV-map. Each pixel in the density map, height map, and intensity map represents the normalized density of the point cloud, the maximum height of the point cloud, and the maximum intensity of the point cloud in that grid point, respectively.

Net (PWF-Net) to filter the feature information of feature points. The experimental results show that PWF-Net and Re-Voxelization Layer enable our method to achieve good detection accuracy for objects with fewer reflection points, such as ‘Cyclist’. In the neck network we improve the spatial semantic feature aggregation (SSFA) module proposed in CIA-SSD [30]. We added feature inputs with different resolutions to further fuse voxel features containing rich local semantic information with projected features in spatial dimension.

In summary, we make three-fold contributions:

- Using point cloud voxelization as an input to compensate for the lack of information after point cloud projection.
- A voxel feature extraction method with variable receptive fields is proposed.
- Improving the SSFA module proposed in CIA-SSD [30] by proposing the Multi-layer Spatial-Semantic Feature Aggregation (MSSFA) module.

II. RELATED WORK

3D object detection based on LiDAR point cloud can be classified into point-based, voxel-based and projection-based methods depending on the data pre-processing method.

A. Point-based 3D object detection methods

Point-based methods usually choose to directly feature extract the raw point cloud and learn the spatial structure features

of the point cloud. But, considering the disorderly nature of point cloud data and other characteristics, such methods usually choose PointNet [20] or PointNet++ [21] for feature extraction. F-PointNet [19] uses the 2D candidate bounding box generated from RGB images to generate a frustum. Then it uses PointNet++ to extract features from the point cloud in the frustum and to perform subsequent classification and regression. PointRCNN [31] is the first point-based two-stage 3D object detection algorithm. It classifies the point cloud in the first stage for foreground and background, then generates 3D candidate bounding box. The second stage further classifies and regresses the detection results of the first stage. STD [32] proposes a two-stage algorithm from sparse to dense, which uses a spherical anchor to generate candidate frames in the first stage to achieve high recall, and a parallel intersection-over-union (IoU) branch in the second stage to achieve high accuracy. PV-RCNN [33] proposes a novel detection framework by combining the advantages of variable perceptual fields of point-based methods with the advantages of efficient feature extraction capabilities of voxel-based methods.

B. Voxel-based 3D object detection method

VoxelNet [34] proposed a method to transform disordered point clouds into regular voxel, then completed the feature extraction and detection tasks with 3D convolution. SECOND [35] proposed a more efficient 3D convolutional feature extraction method called sparse convolution. Voxel R-CNN [36] extends VoxelNet into a two-stage method and proposes the Voxel ROI Pooling method for feature aggregation. PartA² [37] further explores the spatial distribution characteristics of different parts of objects in the annotation frames. It adds the prediction of information about the internal position distribution of foreground objects in the first stage. SA-SSD [38] proposes an auxiliary network that can be turned off anytime to improve the information loss problem due to downsampling in the feature extraction stage. CIA-SSD [30] used IoU-aware confidence rectification module and Multi-task head module to enhance the problem of imbalance between classification confidence and regression confidence in 3D detection tasks. SARPNET [39] compensates for the sparsity and inhomogeneity of point clouds through a uniform sampling method, and enhances the learning of object 3D shape features and spatial semantic features through a shape attention mechanism. DVFENet [40] proposed a two-branch detection method based on an improved voxel graph attention feature extractor (VGAFF) and 3D sparse convolutional networks, which can provide rich 3D feature information. SMS-Net [41] proposed a sparse multi-scale voxel feature aggregation network that divides the raw point cloud into voxels of different sizes to perceive 3D features under different sensory fields.

C. Projection-based 3D object detection method

Projection-based methods usually project disordered point clouds to different viewpoints, transform them into regular pseudo-image representations, and complete subsequent feature extraction and detection tasks with 2D convolution. MV3D, AVOD, etc. [23]–[29], transform the point cloud

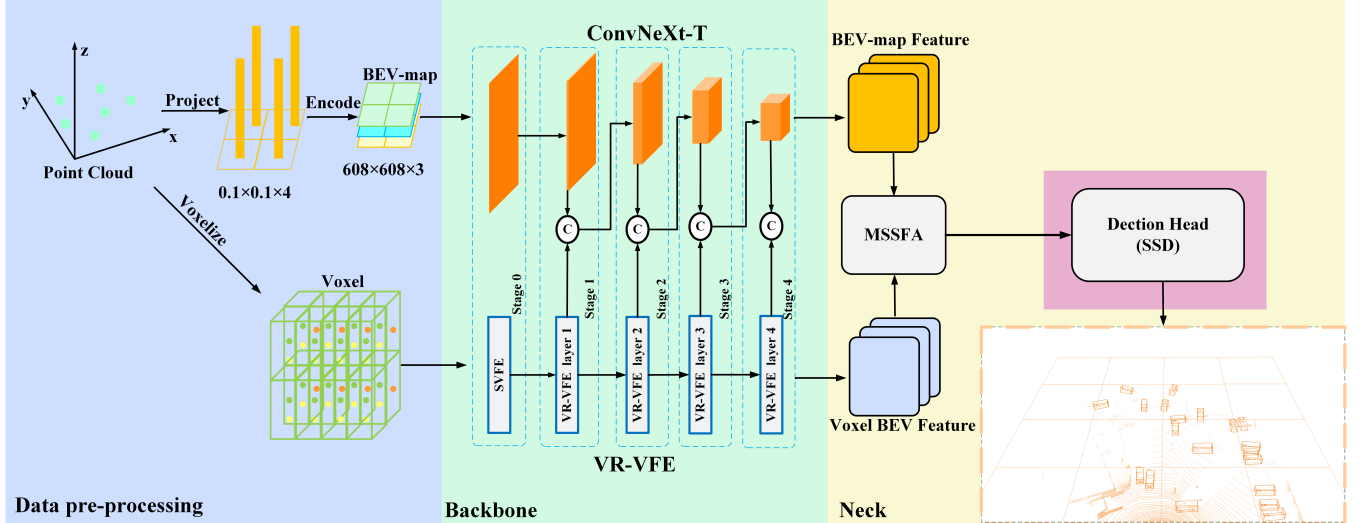


Fig. 2. Algorithm flow. Where 'C' denotes concatenation operation (stitching by feature dimension). The point cloud data are transformed into BEV-map and voxel as input, the BEV-map feature is extracted with ConvNeXt-Tiny, and the voxel features are extracted with VR-VFE proposed in this paper. Multi-scale feature fusion is performed in MSSFA. Finally, the 3D detection is done in SSD Detection Head. ' $0.1 \times 0.1 \times 4$ ' refers to the size of each grid corresponding to reality after meshing the point cloud. ' $608 \times 608 \times 3$ ' refers to the size of the BEV-map generated by the projection.

projection into a height, density, and intensity map for feature extraction. Among them, MV3D and AVOD [25]–[27] use multi-view fusion, while Complex-YOLO and YOLO3D [23], [29] perform feature extraction and detection in a bird's eye view. However, this excessive compression of point cloud information by single view leads to a large amount of feature information loss, which is not conducive to the detection task. PointPillars [28] converts the point cloud into a top-down pillar, then generates a pseudo-image in the bird's-eye view after completing feature encoding on the pillar, which reduces the feature information loss to a certain extent. H²3D-RCNN [25] adopts the same feature encoding method as PointPillars, which combines the advantages of the dense point cloud in perspective view and unobstructed bird's-eye view to improve the detection accuracy further.

III. METHODOLOGY

A. Overview

Fig. 1. shows the form of the data covered in this paper. Fig. 1. (d) shows the BEV-map, while Fig. 1. (e)-(g) display its components; Fig. 1. (a) shows the raw point cloud; Fig. 1. (b) shows the Voxel; Fig. 1. (C) shows the RGB Image. Our method consists of four parts, the flowchart is shown in Fig. 2.

- Data pre-processing: we use two different data pre-processing methods to obtain 2D pseudo-images of the bird's eye view (from now on, we call them BEV-map) and voxelized point cloud data.
- Backbone network: we feed the BEV-map into the 2D convolutional neural network and the voxelized point cloud data into the voxel feature extraction network to complete the feature extraction.
- Neck network: the BEV-map feature and the voxel features are fused with the features.
- Detection head: classify and regress 3D bounding boxes.

B. Data pre-processing

Considering that the farther away from the LiDAR, the sparser the obtained point cloud. Therefore, we selected the point cloud within the range of $x \in [-30.4m, 30.4m]$ and $y \in [0m, 60.8m]$. Considering height of LiDAR above the ground and the problem of occlusion, we selected point cloud within the range of $z \in [-3m, 1m]$. Here we define P_Ω as the set of point clouds, we adopt.

$$P_\Omega = \left\{ P = [x, y, z]^T \right\}$$

$$x \in [0m, 60.8m], y \in [-30.4m, 30.4m], z \in [-3m, 1m] \quad (1)$$

Bev-map: We adopt the same data pre-processing method as Complex-YOLO [22], where the single-frame point cloud data in P_Ω is converted into pseudo-images in bird's-eye view. The maximum height, maximum intensity, and point cloud density in bird's-eye view will be encoded and filled into the corresponding channels. The final size of BEV-map is $608 \times 608 \times 3$, and each pixel corresponds to a realistic range of $[0.1m, 0.1m, 4m]$. The three channels of the BEV-map are encoded by the following (2), (3), and (4).

$$z_g = \max(P_{\Omega i \rightarrow j} \cdot [0, 0, 1]^T) \quad (2)$$

$$z_b = \max(I(P_{\Omega i \rightarrow j})) \quad (3)$$

$$z_r = \min(1.0, \log(N + 1) / \log(64)) \quad N = |P_{\Omega i \rightarrow j}| \quad (4)$$

In the above (2), (3), and (4), z_g represents the maximum height; z_b represents the maximum intensity; z_r represents the normalized density; $I(P_\Omega)$ represents the point cloud intensity; and N represents the number of point clouds in each grid.

Voxel: We will voxelize the single-frame point cloud data in P_Ω , using the same feature encoding as in PointPillars [28]; each point cloud in the voxel will be encoded as a 10-dimensional vector D : $(x, y, z, r, x_c, y_c, z_c, x_p, y_p, z_p)$. where

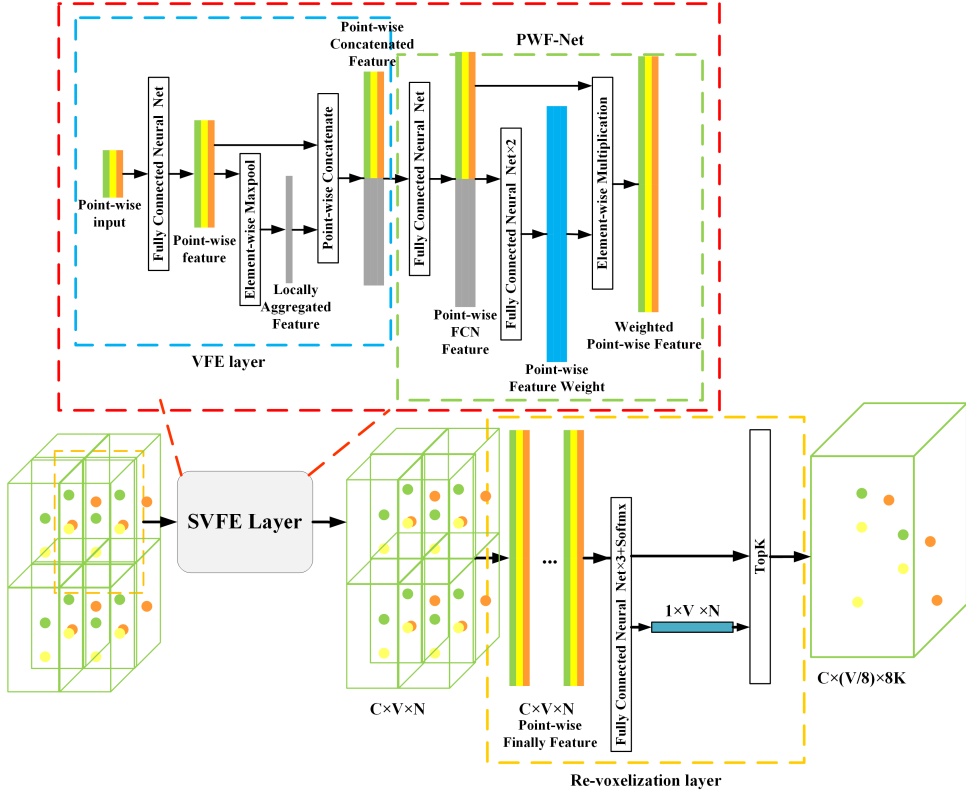


Fig. 3. We present the VR-VFE layer structure with downsampling along the x, y, and z axes. The red dashed box part is SVFE module; the blue dashed box part is VFE module; the green dashed box part is PFW-Net; the yellow dashed box part is Re-voxelization layer. In ' $C \times V \times N$ ', ' V ' denotes the number of voxels, ' N ' denotes that each voxel contains N point-wise, and ' C ' denotes the number of features in each point-wise.

x, y, z, r represent the 3-dimensional coordinates of the point cloud and the reflection intensity, x_c, y_c, z_c represent the geometric centers of all points in the voxel in which the point cloud is located, and x_p, y_p, z_p are $x - x_c, y - y_c, z - z_c$, which represent the relative positions of the points to the geometric centers. Due to the sparsity of the point cloud, most of the sets of voxels are empty, while the non-empty voxels often have only a few points. This sparsity is exploited by imposing limits on the number of non-empty voxels per sample (V) and the number of point clouds per voxel (N) to create a dense tensor of size (D, V, N) . The data will be randomly sampled if a voxel has too many points to fit in this tensor. Conversely, if a voxel has too few points, it will be filled with zeros [28].

C. Backbone

The backbone consists of BEV-map feature extraction network, voxel feature extraction network, and feature fusion.

BEV-map Feature Extraction: We use ConvNeXt [42] as a feature extraction network for BEV-map, which is a feature extraction network proposed by Zhuang Liu et al. in 2022. ConvNeXt made a series of improvements to ResNet [43] by borrowing some module designs from Transformer [44], [45] (e.g., replacing ReLU layer with GeLU layer, replacing Batch Normalize layer with Layer Normalize layer, etc.). In this paper, we use ConvNeXt-Tiny, a lighter version of ConvNext, for feature extraction of BEV-map.

Voxel Feature Extraction: The voxel feature extraction part is stacked by the Variable Receptor Field Voxel Feature

Extraction layer (VR-VFE layer). The VR-VFE layer consists of the modified Stacked Voxel Feature Encoding layer [34] (SVFE layer) and Re-voxelization layer. The structure of VR-VFE layer is shown in Fig. 3. The structure of SVFE is shown in the red dashed box in Fig. 3. The VFE structure is shown in the blue dashed box in Fig. 3. The PFW-Net structure is shown in the green dashed box section of Fig. 3. The Re-voxelization layer structure is shown in the yellow dashed box section of Fig. 3.

SVFE is a voxel feature encoding layer proposed in VoxelNet [34]. The SVFE module used in this paper replaces the original structure with a new one consisting of a VFE layer, a Fully Connected Network layer (FCN, each FCN consists of a fully connected layer, a GeLU layer, and a Layer Normalize layer), and a Point-wise Feature Weighting Net (PWF-Net).

We use $VFE_i(c_{in}, c_{out})$ to represent the VFE layer, where c_{in} represents the input point-wise feature dimension and c_{out} represents the output point-wise feature dimension. Firstly, it raises the feature dimension to $c_{out} \setminus 2$ by FCN to get the point-wise feature. The point-wise feature is then operated by element-wise MaxPool to obtain locally aggregated feature, and finally it is concatenated with the point-wise feature by feature dimension to obtain point-wise concatenated feature with feature dimension c_{out} .

PWF-Net can be seen as a simple self-attention mechanism that enables the network to focus more on features that are beneficial for object detection tasks. It computes the point-wise feature weight (between 0 and 1) using two fully connected

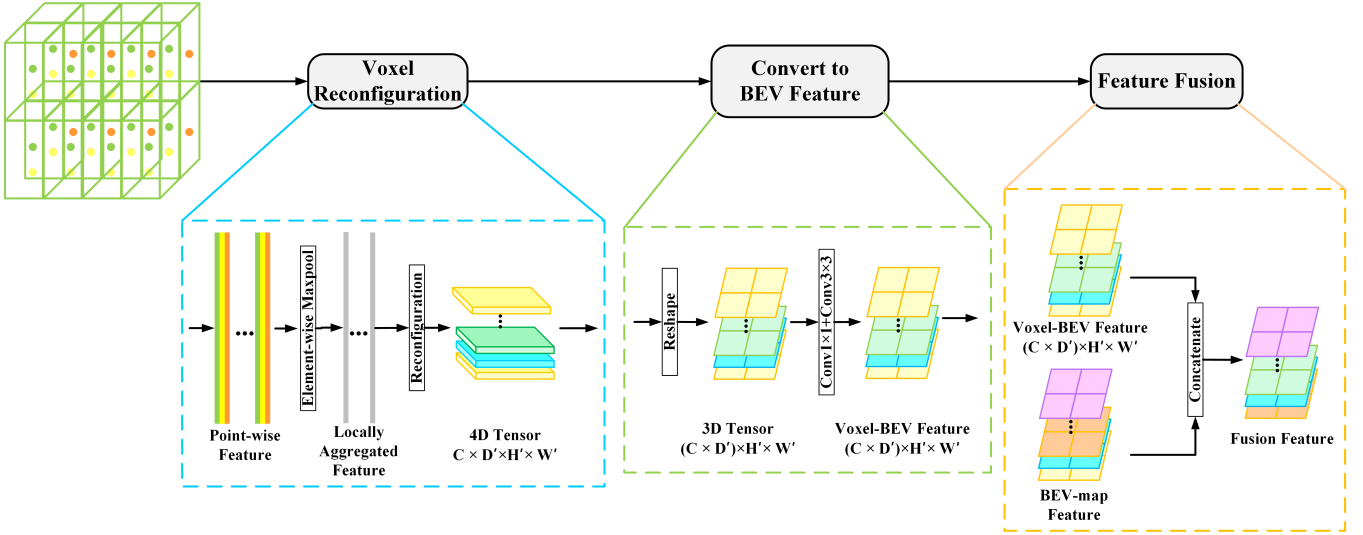


Fig. 4. Feature fusion in the backbone. The blue dashed box shows the process of reconstructing the voxels into a 4D tensor. The green dashed box part transforms the reconstructed 4D tensor into a voxel feature map in the bird's eye view. The yellow dashed box part fuses the BEV-map features with the Voxel BEV features for feature fusion.

layers and a Softmax layer, then multiplies it element-wise with the point-wise FCN feature to obtain the weighted point-wise feature. With this operation, we hope to derive a value between 0 and 1, similar to the contribution of each feature point to the final detection task, and then multiply this contribution value element by element over the feature points to highlight the feature points that are more beneficial to the final detection task. Feature Fusion: In the feature extraction process, we transform the voxelized point-wise features into Voxel-BEV features in the bird's-eye view for feature fusion with BEV-map features. However, each stage in the feature extraction of BEV-map involves a downsampling operation. For example, in ConvNeXt, stage 0 will do 4x downsampling for the feature map. The resolution corresponding to 608×608 in this paper will become 152×152 , while the size of each grid point corresponding to the original point cloud will become $[0.4m, 0.4m, 4m]$. At the same time, the SVFE layer will not change the size of each voxel. Therefore, we designed the Re-voxelization layer to ensure that the Voxel-BEV features at each stage have the same resolution as BEV-map features. On the other hand, as the network deepens, such operations can make the point-wise features in each voxel contain the richer semantic feature.

For the detection task of objects with few reflection points (e.g., cyclists), it is especially important to use a limited number of feature points to complete the feature extraction. In the sampling process, we want to be able to sample each point in the voxel according to its significance for the detection task, so we design a sampling method based on the weight of each point. We obtain the weight value of each point by changing the feature number of the new point-wise feature to 1 through three fully connected layers and changing its value to between 0 and 1 by performing Softmax operation on the feature dimension. Finally, the top K points in each voxel before are selected according to the weight value magnitude as the point-wise in each voxel after the Re-voxelization layer.

For example, if the original voxel contains 12 point-wise points and the voxel size is $[0.1m, 0.1m, 0.125m]$, we hope that after the Re-voxelization layer, each voxel contains 32 point-wise points. After the layer, each voxel contains 32 point-wise, and the voxel size is $[[0.4m, 0.4m, 0.25m]]$. The first 4 points in each voxel will be selected according to the weight value (in this paper, we tend to select more points in the original voxel to increase the robustness of the network and then perform random sampling). After the sampling, to enhance the Point-wise spatial features in the resampled voxels, we encode the (x, y, z, r) of these points corresponding to the points in the original point cloud with the same features as before to obtain $(x, y, z, r, x_c, y_c, z_c, x_p, y_p, z_p)$, and stitch them with point-wise by feature dimension to obtain the new point-wise.

In feature fusion, we first take the point-wise features (stored as (C, V, N)) in the voxels of each stage and get the local features (stored as $(C, 1, N)$) that can represent each voxel through the element-wise MaxPool. The local voxel features are then reconstructed from $(C, 1, N)$ into a sparse 4D tensor of size (C, D', H', W') , where H', W' represents the resolution of voxel features and D' represents the depth of voxel features. This 4D tensor is then reshaped into a 3D tensor of size $((C \times D'), H', W')$, and adjusted to a Voxel-BEV feature with a 1×1 convolution and a 3×3 convolution, and finally, the BEV-map feature obtained from the same Stage as ConvNeXt is stitched by feature dimension. The feature fusion is completed by a 1×1 convolution and a 3×3 convolution, and the subsequent feature extraction is performed. The specific structure is shown in Fig. 4.

D. Neck

In order to detect cars in autonomous driving, it is necessary to regress each car's precise location and classify the bounding box of each regression as positive or negative samples. In such a process, it is crucial to consider both low-level spatial features and high-level abstract semantic features. However,

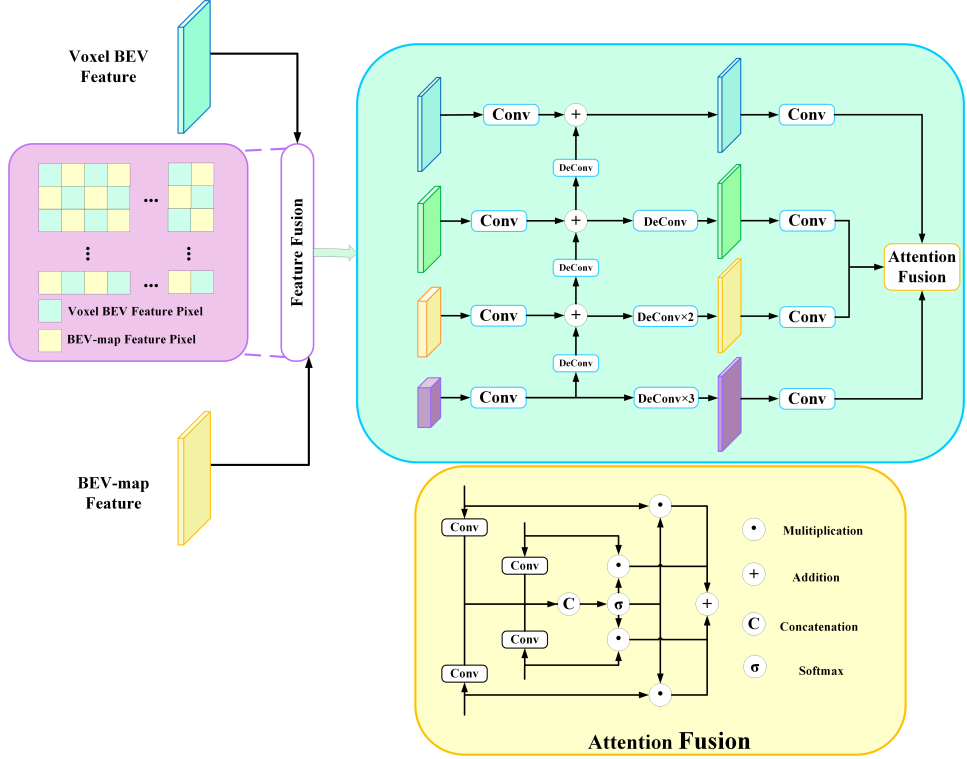


Fig. 5. MSSFA network structure. The purple box is the feature fusion part of Voxel-BEV features and BEV-map features; the blue box is the adjustment part for adjusting the feature map size and feature number; the yellow box is the attention fusion module.

when we enrich the high-level abstract semantic features in the feature map by stacking convolutional layers, the resolution of the feature map gradually decreases, resulting in the loss of spatial information in the high-level feature map. In contrast, the low-level features retain more spatial information but contain less abstract semantic features. In CIA-SSD [30], the SSFA module is proposed for fusing feature information at different levels. In this paper, we improve the SSFA module by 1) adding the fusion of BEV-map feature and voxel BEV feature; 2) using more features with different resolutions as input. We refer to the improved SSFA module as Multi-layers Spatial-Semantic Feature Aggregation module (MSSFA). The structure of MSSFA is shown in Fig. 5.

In the feature extraction stage, we fuse the voxel and BEV-map features with the dimension of the features at the same stage. In the neck part, we fuse voxel-BEV features with BEV-map features in the spatial dimension (i.e., W and H dimensions) for features within the same grid. Firstly, we transform the voxel feature into $((C \times D'), H', W')$ 3D tensor form. Then the number of features is adjusted to be the same as the BEV-map feature in this stage by a 1×1 convolution operation (with C' denoting the adjusted number of features). Then we will create a $((C', 2H', 2W')$ tensor, perform adjacent interpolation operations on Voxel-BEV features with the same index and BEV-map features and complete the feature fusion in the Neck part by one 3×3 and one 1×1 convolution operations. In this paper, we add more levels of feature inputs, using four resolution features as inputs (304×304 , 152×152 , 76×76 , 38×38).

E. Detection Head and Loss function

In this paper, we use the same detection head as PointPillars, with single shot detector (SSD) [46] settings for 3D object detection. We match the prior boxes to the ground truth using 2D Intersection over Union (IoU) [47]. Bounding box height and elevation were not used for matching; instead given a 2D match, the height and elevation become additional regression targets.

The loss function we use the same loss function as SEC-OND [35] and PointPillars [28]. Ground truth boxes and anchors are defined by $(x, y, z, w, l, h, \theta)$. The localization regression residuals between ground truth boxes and anchors are defined as (5).

$$\begin{aligned} \Delta x &= \frac{x^{gt} - x^a}{d^a}, \Delta y = \frac{y^{gt} - y^a}{d^a}, \Delta z = \frac{z^{gt} - z^a}{d^a} \\ \Delta w &= \log \frac{w^{gt}}{w^a}, \Delta l = \log \frac{l^{gt}}{l^a}, h = \Delta \log \frac{h^{gt}}{h^a} \end{aligned} \quad (5)$$

Where x^{gt} , x^a denote ground truth and anchor boxes, respectively; $d^a = \sqrt{(w^a)^2 + (l^a)^2}$. The total localization loss can then be defined as:

$$L_{loc} = \sum_{b \in (x, y, z, w, h, l)} SmoothL1(\Delta b) \quad (6)$$

We choose Focal loss [48] as the loss function for object classification. Where θ_t is the true value of the object orientation angle and θ_{gt} is the predicted value of the object orientation angle.

$$L_{cls} = -\theta_t \log(\theta_{gt}) - (1 - \theta_t) \log(1 - \theta_{gt}) \quad (7)$$

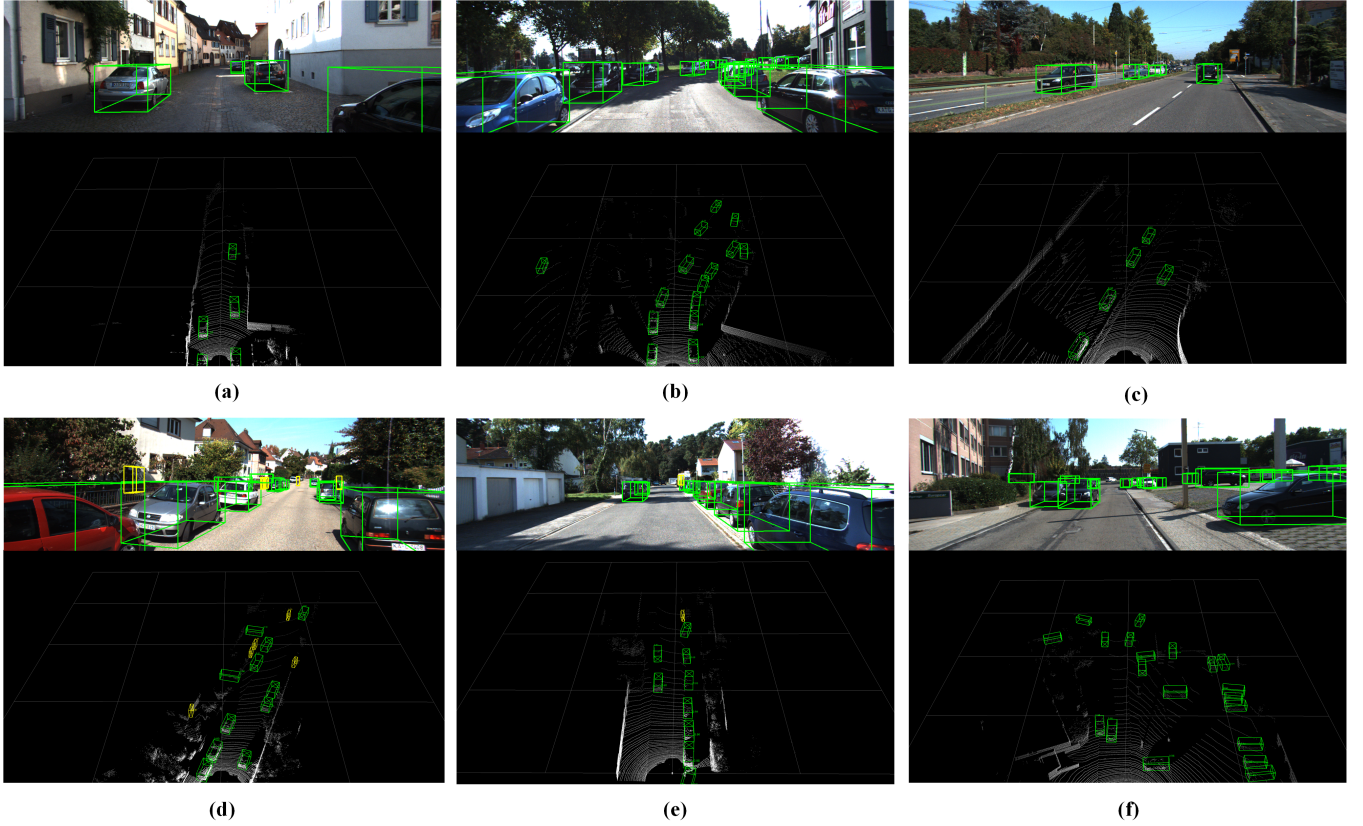


Fig. 6. Qualitative analysis of KITTI results. The bottom half is the 3D bounding boxes on the point cloud. The upper part is the 3D bounding box projected into the image for a clearer view. Note that our method uses only LiDAR. We show the predicted boxes for ‘Car’ class (green) and ‘Cyclist’ class (yellow).

We choose Cross Entropy loss as the regression loss function for the object orientation angle.

$$L_{cls} = -\alpha_a (1 - p^\alpha)^\gamma \log(p^\alpha) \quad (8)$$

Where p^α is the category probability of an anchor box. We use the parameter settings of $\alpha = 0.25$ and $\gamma = 2$ from the original paper. Thus, the total loss is as shown in (9). Where N_{pos} represents the number of positive samples, while $\beta_{loc} = 2, \beta_{cls} = 1, \beta_{dir} = 0.2$.

$$L = \frac{1}{N_{pos}} (\beta_{loc} L_{loc} + \beta_{dir} L_{dir} + \beta_{cls} L_{cls}) \quad (9)$$

IV. EXPERIMENTS AND RESULTS

A. Datasets

We evaluated our method on the KITTI 3D object benchmark dataset [53]. The KITTI dataset has 7,481 training samples and 7,518 test samples. The training samples were divided into a training set (3,712 samples) and a validation set (3,769 samples). We conducted experiments on the most commonly used ‘Car’ and ‘Cyclist’ classes and evaluated the results by average precision (AP) and IoU thresholds (0.7 for cars and 0.5 for bicycles). Also, the dataset has three difficulty levels (easy, medium, and hard) based on object size, occlusion, and truncation levels. Fig. 6 shows the results of our predictions.

B. Implementation Details

We project the point cloud data in the range of $[0m, 60.8m]$, $[-30.4m, 30.4m]$. The point cloud data in the range of $[-3m, 1m]$ (along the x-axis, y-axis, and z-axis) is projected to the bird’s-eye view to construct a 608×608 BEV-map with each pixel corresponding to a realistic size of $[0.1m, 0.1m]$. The size of each voxel after voxelization is $[0.1m, 0.1, 0m, 125m]$, and the number of point clouds is 12. The size of the anchor box of the ‘Car’ class is $[3.9m, 1.6m, 1.56m]$ (the center of the z-axis is -1.78), and the size of the anchor box of the ‘Cyclist’ class is $[1.76m, 0.6m, 1.73m]$ (the center of the z-axis is -0.6). The anchor is set for two possible orientations 0° and 90° . In addition, according to the matching strategy in VoxelNet [33], the samples were classified as positive, negative, and ignored according to the IoU threshold (0.6 and 0.45 for ‘Car’ class and 0.5 and 0.35 for ‘Cyclist’ class).

For the data augmentation part, we first created a look-up table of ground truth 3D boxes for all categories and the associated point clouds that fall within these 3D boxes, following the approach of SECOND [35]. Then, for each sample, we randomly selected 15 ground truth samples for ‘Car’ class and 15 for ‘Cyclist’ class, respectively, and placed them into the current point cloud. Next, these ground truth boxes are individually augmented with data. Each ground truth box was randomly rotated (drawn from $[-\pi/4, \pi/4]$) and translated (x, y, and z values were randomly drawn

TABLE I

THE 3D DETECTION RESULTS ON THE KITTI TEST SET FOR CAR AND CYCLIST CLASSES USING AP@R40. “L” AND “I+L” INDICATE THE APPLICATION OF LIDAR POINT CLOUDS, RGB IMAGES, AND A FUSION OF RGB IMAGES AND LIDAR, RESPECTIVELY. NOTE THAT WE ONLY COMPARED WITH THE 3D DETECTION PART OF DIFI.

Method	Input	Car $AP_{Bev}(\%)$			Cyclist $AP_{Bev}(\%)$			Car $AP_{3D}(\%)$			Cyclist $AP_{3D}(\%)$		
		Easy	Mod.	Hard	Easy	Mod.	Hard	Easy	Mod.	Hard	Easy	Mod.	Hard
MV3D [27]	L+I	86.02	76.90	68.49	N/A	N/A	N/A	71.09	62.35	55.12	N/A	N/A	N/A
Cont-Fuse [49]	L+I	88.81	85.83	77.33	N/A	N/A	N/A	82.54	66.22	64.04	N/A	N/A	N/A
Roarnet [50]	L+I	88.20	79.41	70.02	N/A	N/A	N/A	83.71	73.04	59.16	N/A	N/A	N/A
DIFI [51]	L+I	91.01	87.51	84.25	N/A	N/A	N/A	85.29	76.59	71.75	N/A	N/A	N/A
AVOD [26]	L+I	88.53	83.79	77.90	68.09	57.48	50.77	81.84	71.88	66.38	64.00	52.18	46.61
F-PoinNet [19]	L+I	88.70	84.00	75.33	75.38	61.96	54.68	81.20	70.39	62.19	71.69	56.77	50.9
MSL3D [51]	L+I	N/A	N/A	N/A	N/A	N/A	N/A	87.27	81.15	76.56	76.74	62.27	56.20
SMS-Net [41]	L	N/A	N/A	N/A	N/A	N/A	N/A	87.01	76.21	70.45	75.35	60.23	53.37
CIA-SSD [30]	L	N/A	N/A	N/A	N/A	N/A	N/A	89.59	80.28	72.89	N/A	N/A	N/A
Fast Point-RCNN [52]	L	90.87	87.84	80.52	68.09	57.48	50.77	85.29	77.40	70.24	N/A	N/A	N/A
SA-SSD [38]	L	95.03	91.03	85.96	75.38	61.96	54.68	88.75	79.79	74.16	N/A	N/A	N/A
Part-A ² [37]	L	91.70	87.79	84.61	83.43	68.73	61.85	87.81	78.49	73.51	79.17	63.52	56.93
PV-RCNN [33]	L	94.98	90.65	86.14	82.49	68.89	62.41	90.25	81.43	76.82	78.60	63.71	57.65
PointRCNN [31]	L	92.13	87.39	82.72	82.56	67.24	60.28	86.96	75.64	70.70	74.96	58.82	52.53
STD [32]	L	94.74	89.19	86.42	81.36	67.23	59.35	87.95	79.91	75.09	78.69	61.59	55.30
SECOND [35]	L	88.07	79.37	77.95	73.67	56.04	48.78	83.13	73.66	66.20	70.51	53.85	46.90
PointPillars [28]	L	88.35	86.10	79.83	79.14	62.25	56.00	79.05	74.99	68.30	75.78	59.07	52.92
H ² 3D R-CNN [25]	L	82.85	88.87	86.07	82.76	67.90	60.49	90.43	81.55	77.22	78.67	62.74	55.78
DVFENet [40]	L	90.93	87.68	84.60	82.29	67.40	60.71	86.20	79.18	74.58	78.73	62.00	55.18
SARPNET [39]	L	88.93	87.26	78.68	79.94	62.80	55.86	84.92	75.64	67.70	77.66	60.43	54.03
Ours	L	91.32	87.46	84.38	81.58	66.93	60.21	86.71	78.53	74.09	78.84	63.00	55.85

TABLE II

THE 3D DETECTION RESULTS ON THE KITTI TEST SET FOR CAR AND CYCLIST CLASSES USING AP@R40. “L” AND “I+L” INDICATE THE APPLICATION OF LIDAR POINT CLOUDS, RGB IMAGES, AND A FUSION OF RGB IMAGES AND LIDAR, RESPECTIVELY. NOTE THAT WE ONLY COMPARED WITH THE 3D DETECTION PART OF DIFI.

Method	Modality	Car $AP_{Bev}(\%)$			Cyclist $AP_{Bev}(\%)$			Car $AP_{3D}(\%)$			Cyclist $AP_{3D}(\%)$		
		Easy	Mod.	Hard	Easy	Mod.	Hard	Easy	Mod.	Hard	Easy	Mod.	Hard
Complex-YOLO [23]	Lidar	85.89	77.40	77.33	72.37	63.36	60.27	67.72	64.00	63.01	68.17	58.32	54.30
Ours	Lidar	90.11	87.93	85.28	82.35	72.18	67.29	88.53	77.80	75.82	84.73	70.17	66.33

from [0, 0.5]). Finally, two sets of global data augmentation are performed, a random mirror flip along the x-axis [54] and a global scaling [34], [35] (scaling is randomly drawn from [0.95, 1.05]). Please refer to OpenPCDet¹ for the specific configuration. We implemented the method of this paper using OpenPCDet and completed all the experiments.

For the feature extraction network of BEV-map we have chosen ConvNeXt-Tiny [42]. The voxel feature extraction network is stacked by VR-VFE layer. In the MSSFA module, we take the outputs of Stage1, Stage2, Stage3, and Stage4 of the feature voxel extraction network as its input (corresponding to resolutions of 152×152, 76×76, 38×38, 19×19). The BEV-map feature and Voxel BEV feature of the same stage perform adjacent interpolation operations. Then the output is adjusted for the number of channels with a 1×1 convolution with 256 output channels, and the features are fused with a 3×3 convolution with stride of 1 and padding of 1. The 2D DeConv layer consists of a 3×3 convolution and a 3×3 deconvolution. In attention fusion, a 3×3 convolution is performed with an output channel of 1 to obtain the attention map. The head network settings obey the settings in PointPillars [?].

We merged the validation set of the KITTI dataset with

the training set to construct a new training set (3,712 samples in the original training set and 3,769 samples in the original validation set, with a total of 7,481 samples in the combined training set). The ADAM optimizer [55] and OnecycleLR [56] were applied to train 100 epochs on RTX3090 with the initial learning rate set to 0.003, weight decay to 0.01, and momentum to 0.9.

C. Compared with Others

All detection results were measured using the official KITTI evaluation detection metrics of bird’s eye view (BEV), 3D, 2D, and average orientation similarity (AOS). 2D detection was performed in the image plane; AOS evaluates the average direction of 2D detection (measured by BEV, IoU threshold of 0.7 for ‘Car’ class and 0.5 for ‘Cyclist’ class). The experimental results are shown in Table I and II.

Table I shows the 3D detection AP and BEV detection AP of our method on the KITTI test set. In both tables, we classify these methods into two categories based on the type of sensor used (methods such as MV3D use both camera and Lidar, while methods such as PV-RCNN use Lidar). From the table, we can see that our method’s AP for ‘Car’ class performs poorly, with 3D AP of 86.71%, 78.53%, and 74.09% under Easy, Mod, and Hard conditions, respectively, which

¹<https://github.com/open-mmlab/OpenPCDet>

TABLE III

PERFORMANCE COMPARISON ON THE KITTI VAL SET, WITH AP CALCULATED BY 11 RECALL POSITIONS FOR CAR AND CYCLIST. ‘BEV’, ‘VOXEL’, ‘PWF-NET’, ‘MSSFA’, ‘RE-VOXELIZATION LAYER’, ‘RE-VOXELIZATION LAYER (RANDOMLY SAMPLE)’ DENOTE BEV-MAP AS INPUT; VOXEL AS INPUT; PWF-NET MODULE PROPOSED IN THIS PAPER; MSSFA MODULE PROPOSED IN THIS PAPER; THE RE-VOXELIZATION LAYER PROPOSED IN THIS PAPER; THE RE-VOXELIZATION LAYER WITH RANDOM SAMPLING INSTEAD OF SAMPLING BY POINT WEIGHTS. BOLDED VALUES ARE THE BEST PERFORMANCES FOR ALL METHODS.

Improved Part	Method A	Method B	Method C	Method D	Method E
BEV	✓		✓	✓	✓
Voxel		✓	✓	✓	✓
PWF-Net				✓	✓
MSSFA	✓	✓	✓	✓	✓
Re-voxelization layer					✓
Re-voxelization layer(Randomly Sample)		✓	✓	✓	
Car AP	Easy	80.61	89.36	89.77	89.80
BEV Detection (IoU=0.7)	Mod.	66.83	87.00	87.80	87.52
	Hard	64.22	82.55	83.62	82.44
Cyclist AP	Easy	54.46	78.03	83.02	83.18
BEV Detection (IoU=0.5)	Mod.	42.66	64.39	67.20	69.75
	Hard	41.44	60.41	66.88	65.76
Car AP	Easy	62.15	85.76	87.61	87.45
3D Detection (IoU=0.7)	Mod.	52.11	75.96	76.43	76.88
	Hard	50.00	71.18	72.44	71.44
Cyclist AP	Easy	44.00	76.37	80.00	82.02
3D Detection (IoU=0.5)	Mod.	42.12	59.63	66.20	67.65
	Hard	39.25	57.33	62.15	63.00
					90.11
					87.93
					85.28
					85.35
					72.18
					67.29
					88.53
					77.80
					75.82
					84.73
					70.17
					66.33

TABLE IV

ANALYSIS OF THE MULTI FEATURES FUSION OPERATION. NOTATION: ‘SP’ REPRESENTS THE FEATURE FUSION MODULE IN THE MSSFA PROPOSED IN THIS PAPER. BOLDED VALUES ARE THE BEST PERFORMANCES FOR ALL METHODS.

Method	BEV	Feature Voxel	Fusion SP	Concat	Mod. AP _{3D} (%)	
					Car	Cyclist
A	✓				52.11	42.12
B		✓			75.96	59.63
F	✓	✓		✓	75.49	62.29
C	✓	✓	✓	✓	76.43	66.20

has a certain gap with advanced methods such as PV-RCNN. However, compared with projection-based 3D object detection methods [26]–[28], our method all have good advantages. For the ‘Cyclist’ class AP, our method has good performance. The 3D AP for ‘Cyclist’ class is 78.84%, 63.00%, and 55.85%.

As can be seen from Table I, our method has 3% lower 3D AP in the ‘Car’ class compared to the H²3D R-CNN [25], which is also based on the projection method. After our analysis, the reasons are: (1) The H23D R-CNN uses a dynamic voxelization feature coding method [57], establishing a complete mapping relationship between points and voxels. In contrast, this paper uses a hard voxelization approach [34], which leads to uncertain voxel filling and information loss due to random sampling and discarding operations. (2) The projected features in the H23D R-CNN retain higher dimensional feature information through the MLP layer. In contrast, this paper uses the same feature coding method as

Complex-YOLO [23], which over-compresses the features in the bird’s-eye view, resulting in information loss. (3) H23D R-CNN is a two-stage 3D detector that fully uses the prior knowledge of the Region Proposal Network (RPN) module. In contrast, the method in this paper is a one-stage 3D detector, and the detection accuracy depends heavily on how well the features are extracted. However, we found that our method has good accuracy for objects with fewer reflection points like cyclist. We analyzed the main reasons for this as: (1) However, the hard voxelization we use causes some information loss, we use a weight-based feature point sampling method in the Re-voxelization layer proposed in this paper. For objects with fewer reflective points, such as cyclists, we can prioritize the feature points that are more beneficial to the detection task. (2) PWF-Net can filter out the point feature information more beneficial to the detection task. (3) For objects with few reflection points and small sizes, like the ‘Cyclist’ class, the voxel description in 3D space is more responsive to its features than the 2D perspective view. In the MSSFA module, we complemented the BEV-map features with voxel BEV features at the same grid points. In the subsequent ablation experiments, we can also see that the Re-voxelization layer, PWF-Net and the feature fusion module in MSSFA have a good improvement of the detection accuracy for the ‘Cyclist’ class.

Table II shows the results of our comparison with Complex-YOLO [23]. Considering that the detection results for the KITTI test set are not submitted in Complex-YOLO, we compared our method with Complex-YOLO on the val set of KITTI. In this paper, the same bird’s-eye view projection

encoding method as Complex-YOLO is used. As can be seen in Table II, our method is more advantageous in both BEV AP and 3D AP. Although in 3D detection, Complex-YOLO does not predict the height of the object, which affects the accuracy of 3D detection to some extent, our method has a greater improvement compared with it in the BEV detection results.

D. Ablation Experiment

To further validate the validate the effectiveness of each part of our method, we performed further validation on the validation set of the KITTI dataset. All experiments were performed on the same data set division (3,712 samples for the training set and 3,769 samples for the validation set), using the same parameter configuration and 100 epochs trained on RTX3090. The experimental results are shown in Table III.

Method A: Method A uses BEV-map as input and ConvNeXt-Tiny for feature extraction. Because only BEV-map is used as is input, the feature fusion part is removed from the MSSFA module that is not available in Method A. The resolution of BEV-map is 608×608, and the used point cloud range is [60.8m, 60.8m, 4m]. The rest of the settings are the same as the method proposed in this paper. As can be seen from Table III, the detection results obtained by using only BEV-map as input are poor. This is because projecting the point cloud to the bird's view causes more information loss in the data processing stage, which is not beneficial for the subsequent detection tasks.

Method B: Method B uses voxel as input, and a voxel feature extraction network constructed by stacking SVFE and Re-voxelization (Randomly Sample) layer is used for feature extraction. Because only voxel is used as input, the feature fusion part is removed from the MSSFA module that is not available in Method B. The used point cloud range is [60.8m, 60.8m, 4m]. The size of each voxel is [0.1m, 0.1, 0m, 125m], and each voxel is randomly sampled with 12 points. The rest of the settings are the same as the method proposed in this paper. Compared with Method A, the voxel can retain more point cloud information, and the Re-voxelization layer is designed to achieve feature interaction of adjacent voxels. Compared with Method A, the detection accuracy of Method B is greatly improved.

Method C: Method C uses a mixture of BEV-map and voxel as input. Compared with methods A and B, the fusion of voxel and BEV-map features was added to the MSSFA module. BEV-map and voxel have the same parameters as methods A and B. The rest of the settings are the same as the method proposed in this paper. The detection accuracy has been improved compared to Method A and Method B (compared to Method A, 3D AP of 'Car' class is improved by 25.46%, 24.32%, 22.44%, 3D AP of 'Cyclist' class is improved by 36%, 22.08%, 22.9%; compared to Method B, 3D AP of 'Car' class is improved by 1.85%, 0.47%, 0.56%, 3D AP of 'Cyclist' class is improved by 3.63%, 6.57%, and 4.82%).

Method D: Method D adds PWF-Net to Method C. The rest of the settings are the same as the method proposed in

this paper. Compared to Method C, Method D has improved detection accuracy in 'Cyclist' class (compared to Method C, 3D AP of 'Car' class is improved by 2.02%, 1.35%, 0.85%, 3D AP of 'Cyclist' class is improved by 2.02%, 1.35%, 0.85%).

Method E: Method E (the method proposed in this paper) replaces random sampling with perpoint weight sampling. Compared with Method D, the detection accuracy of Method E is improved more in the detection accuracy of small objects like cyclist with fewer point clouds (compared with Method D, the 3D AP of 'Car' is improved by 1.08%, 0.92%, 4.38%, the 3D AP of 'Cyclist' class is improved by 4.71%, 2.52%, 3.33%).

By comparing Method A and C, we can find that voxel can be used to compensate for the information loss of the point cloud during projection. Compared with Method B, Method C adds point cloud projection as input, which can also help the final detection task. The comparison between Method C, D, and E shows that the PWF-Net and the Re-voxelization layer sampled by weight are good for detecting objects with few reflection points like cyclist. This is because, for objects with fewer points, the Re-voxelization layer with weight sampling and PWF-Net can filter out the feature points that are more beneficial for the detection task.

In the MSSFA module, we added the feature fusion module for Voxel-BEV and BEV-map feature fusion. To verify the effectiveness of our feature fusion module design, we designed the corresponding comparison experiments. Table IV shows the experimental results. Method A, B, and C, in Table IV, corresponding to the methods mentioned in Table III. We modify the feature fusion module in MSSFA to Concat operation (i.e., stitching by feature dimension) in Method F. The rest of the module design in Method F is the same as Method C. As we can see from Table IV, compared to Method F, Method C has improved 3D AP in Mod. conditions ('Car':0.94%, 'Cyclist':3.91%). The 3D AP of 'Car' and 'Cyclist' are also improved by Method F under Mod. conditions compared to Method A, B ('Car': 23% compared to Method A, B, 'Cyclist': 20.17%, 2.66%; 'Car' by 23.38%, -0.47%, respectively).

REFERENCES

- [1] W. Zhou, S. Pan, J. Lei, and L. Yu, "Tmfnet: Three-input multilevel fusion network for detecting salient objects in rgb-d images," *IEEE Transactions on Emerging Topics in Computational Intelligence*, vol. 6, no. 3, pp. 593–601, 2021.
- [2] R. Barkur, D. Suresh, S. Lal, C. S. Reddy, P. Diwakar *et al.*, "Rscdnet: A robust deep learning architecture for change detection from bi-temporal high resolution remote sensing images," *IEEE Transactions on Emerging Topics in Computational Intelligence*, vol. 7, no. 2, pp. 537–551, 2022.
- [3] R. Cong, W. Song, J. Lei, G. Yue, Y. Zhao, and S. Kwong, "Psnet: Parallel symmetric network for video salient object detection," *IEEE Transactions on Emerging Topics in Computational Intelligence*, vol. 7, no. 2, pp. 402–414, 2022.
- [4] Y. Li, C. Pan, X. Cao, and D. Wu, "Power line detection by pyramidal patch classification," *IEEE Transactions on Emerging Topics in Computational Intelligence*, vol. 3, no. 6, pp. 416–426, 2018.
- [5] L. Chen, X. Jiang, X. Liu, T. Kirubarajan, and Z. Zhou, "Outlier-robust moving object and background decomposition via structured ℓ_p -regularized low-rank representation," *IEEE Transactions on Emerging Topics in Computational Intelligence*, vol. 5, no. 4, pp. 620–638, Aug 2021.

[6] J. Chen, H. Chen, Y. Guo, M. Zhou, R. Huang, and C. Mao, "A novel test case generation approach for adaptive random testing of object-oriented software using k-means clustering technique," *IEEE Transactions on Emerging Topics in Computational Intelligence*, vol. 6, no. 4, pp. 969–981, 2021.

[7] A. Pramanik, S. K. Pal, J. Maiti, and P. Mitra, "Granulated rcnn and multi-class deep sort for multi-object detection and tracking," *IEEE Transactions on Emerging Topics in Computational Intelligence*, vol. 6, no. 1, pp. 171–181, 2021.

[8] H. Wang, Y. Xu, Z. Wang, Y. Cai, L. Chen, and Y. Li, "Centernet-auto: A multi-object visual detection algorithm for autonomous driving scenes based on improved centernet," *IEEE Transactions on Emerging Topics in Computational Intelligence*, 2023.

[9] W. Zhou, Y. Zhu, J. Lei, J. Wan, and L. Yu, "Apnet: Adversarial learning assistance and perceived importance fusion network for all-day rgb-t salient object detection," *IEEE Transactions on Emerging Topics in Computational Intelligence*, vol. 6, no. 4, pp. 957–968, 2021.

[10] X. Chen, K. Kundu, Y. Zhu, A. G. Berneshawi, H. Ma, S. Fidler, and R. Urtasun, "3d object proposals for accurate object class detection," *Advances in neural information processing systems*, vol. 28, 2015.

[11] Z. Deng and L. Jan Latecki, "Amodal detection of 3d objects: Inferring 3d bounding boxes from 2d ones in rgb-depth images," in *Proceedings of the IEEE Conference on Computer Vision and Pattern Recognition*, 2017, pp. 5762–5770.

[12] D. Xu, W. Ouyang, E. Ricci, X. Wang, and N. Sebe, "Learning cross-modal deep representations for robust pedestrian detection," in *Proceedings of the IEEE conference on computer vision and pattern recognition*, 2017, pp. 5363–5371.

[13] S. Gupta, R. Girshick, P. Arbeláez, and J. Malik, "Learning rich features from rgb-d images for object detection and segmentation," in *Computer Vision–ECCV 2014: 13th European Conference, Zurich, Switzerland, September 6–12, 2014, Proceedings, Part VII 13*. Springer, 2014, pp. 345–360.

[14] J. Sun, L. Chen, Y. Xie, S. Zhang, Q. Jiang, X. Zhou, and H. Bao, "Disp r-cnn: Stereo 3d object detection via shape prior guided instance disparity estimation," in *Proceedings of the IEEE/CVF conference on computer vision and pattern recognition*, 2020, pp. 10 548–10 557.

[15] Y. Chen, S. Liu, X. Shen, and J. Jia, "Dsgn: deep stereo geometry network for 3d object detection, 2020 ieee," in *CVF conference on computer vision and pattern recognition (CVPR)*, 2020, pp. 12 533–12 542.

[16] J.-R. Chang and Y.-S. Chen, "Pyramid stereo matching network," in *Proceedings of the IEEE conference on computer vision and pattern recognition*, 2018, pp. 5410–5418.

[17] P. Li, X. Chen, and S. Shen, "Stereo r-cnn based 3d object detection for autonomous driving," in *Proceedings of the IEEE/CVF Conference on Computer Vision and Pattern Recognition*, 2019, pp. 7644–7652.

[18] C. Nie, Z. Ju, Z. Sun, and H. Zhang, "3d object detection and tracking based on lidar-camera fusion and imm-ukf algorithm towards highway driving," *IEEE Transactions on Emerging Topics in Computational Intelligence*, 2023.

[19] C. R. Qi, W. Liu, C. Wu, H. Su, and L. J. Guibas, "Frustum pointnets for 3d object detection from rgb-d data," in *Proceedings of the IEEE conference on computer vision and pattern recognition*, 2018, pp. 918–927.

[20] C. R. Qi, H. Su, K. Mo, and L. J. Guibas, "Pointnet: Deep learning on point sets for 3d classification and segmentation," in *Proceedings of the IEEE conference on computer vision and pattern recognition*, 2017, pp. 652–660.

[21] C. R. Qi, L. Yi, H. Su, and L. J. Guibas, "Pointnet++: Deep hierarchical feature learning on point sets in a metric space," *Advances in neural information processing systems*, vol. 30, 2017.

[22] T. Guan, J. Wang, S. Lan, R. Chandra, Z. Wu, L. Davis, and D. Manocha, "M3detr: Multi-representation, multi-scale, mutual-relation 3d object detection with transformers," in *Proceedings of the IEEE/CVF Winter Conference on Applications of Computer Vision (WACV)*, January 2022, pp. 772–782.

[23] M. Simony, S. Milzy, K. Amendey, and H.-M. Gross, "Complex-yolo: An euler-region-proposal for real-time 3d object detection on point clouds," in *Proceedings of the European conference on computer vision (ECCV) workshops*, 2018, pp. 0–0.

[24] Y. Shao, Z. Sun, A. Tan, and T. Yan, "Efficient three-dimensional point cloud object detection based on improved complex-yolo," *Frontiers in NeuroRobotics*, vol. 17, p. 1092564, 2023.

[25] J. Deng, W. Zhou, Y. Zhang, and H. Li, "From multi-view to hollow-3d: Hallucinated hollow-3d r-cnn for 3d object detection," *IEEE Transactions on Circuits and Systems for Video Technology*, vol. 31, no. 12, pp. 4722–4734, 2021.

[26] J. Ku, M. Mozifian, J. Lee, A. Harakeh, and S. L. Waslander, "Joint 3d proposal generation and object detection from view aggregation," in *2018 IEEE/RSJ International Conference on Intelligent Robots and Systems (IROS)*. IEEE, 2018, pp. 1–8.

[27] X. Chen, H. Ma, J. Wan, B. Li, and T. Xia, "Multi-view 3d object detection network for autonomous driving," in *Proceedings of the IEEE conference on Computer Vision and Pattern Recognition*, 2017, pp. 1907–1915.

[28] A. H. Lang, S. Vora, H. Caesar, L. Zhou, J. Yang, and O. Beijbom, "Pointpillars: Fast encoders for object detection from point clouds," in *Proceedings of the IEEE/CVF conference on computer vision and pattern recognition*, 2019, pp. 12 697–12 705.

[29] W. Ali, S. Abdelkarim, M. Zidan, M. Zahran, and A. El Sallab, "Yolo3d: End-to-end real-time 3d oriented object bounding box detection from lidar point cloud," in *Proceedings of the European conference on computer vision (ECCV) workshops*, 2018, pp. 0–0.

[30] W. Zheng, W. Tang, S. Chen, L. Jiang, and C.-W. Fu, "Cia-ssd: Confident iou-aware single-stage object detector from point cloud," in *Proceedings of the AAAI conference on artificial intelligence*, vol. 35, no. 4, 2021, pp. 3555–3562.

[31] S. Shi, X. Wang, and H. Li, "Pointrcnn: 3d object proposal generation and detection from point cloud," in *Proceedings of the IEEE/CVF conference on computer vision and pattern recognition*, 2019, pp. 770–779.

[32] Z. Yang, Y. Sun, S. Liu, X. Shen, and J. Jia, "Std: Sparse-to-dense 3d object detector for point cloud," in *Proceedings of the IEEE/CVF international conference on computer vision*, 2019, pp. 1951–1960.

[33] S. Shi, C. Guo, L. Jiang, Z. Wang, J. Shi, X. Wang, and H. Li, "Pv-rcnn: Point-voxel feature set abstraction for 3d object detection," in *Proceedings of the IEEE/CVF conference on computer vision and pattern recognition*, 2020, pp. 10 529–10 538.

[34] Y. Zhou and O. Tuzel, "Voxelenet: End-to-end learning for point cloud based 3d object detection," in *Proceedings of the IEEE conference on computer vision and pattern recognition*, 2018, pp. 4490–4499.

[35] Y. Yan, Y. Mao, and B. Li, "Second: Sparsely embedded convolutional detection," *Sensors*, vol. 18, no. 10, p. 3337, 2018.

[36] J. Deng, S. Shi, P. Li, W. Zhou, Y. Zhang, and H. Li, "Voxel r-cnn: Towards high performance voxel-based 3d object detection," in *Proceedings of the AAAI Conference on Artificial Intelligence*, vol. 35, no. 2, 2021, pp. 1201–1209.

[37] S. Shi, Z. Wang, J. Shi, X. Wang, and H. Li, "From points to parts: 3d object detection from point cloud with part-aware and part-aggregation network," *IEEE transactions on pattern analysis and machine intelligence*, vol. 43, no. 8, pp. 2647–2664, 2020.

[38] C. He, H. Zeng, J. Huang, X.-S. Hua, and L. Zhang, "Structure aware single-stage 3d object detection from point cloud," in *Proceedings of the IEEE/CVF conference on computer vision and pattern recognition*, 2020, pp. 11 873–11 882.

[39] Y. Ye, H. Chen, C. Zhang, X. Hao, and Z. Zhang, "Sarpenet: Shape attention regional proposal network for lidar-based 3d object detection," *Neurocomputing*, vol. 379, pp. 53–63, 2020.

[40] Y. He, G. Xia, Y. Luo, L. Su, Z. Zhang, W. Li, and P. Wang, "Dvfenet: Dual-branch voxel feature extraction network for 3d object detection," *Neurocomputing*, vol. 459, pp. 201–211, 2021.

[41] S. Liu, W. Huang, Y. Cao, D. Li, and S. Chen, "Sms-net: Sparse multi-scale voxel feature aggregation network for lidar-based 3d object detection," *Neurocomputing*, vol. 501, pp. 555–565, 2022.

[42] Z. Liu, H. Mao, C.-Y. Wu, C. Feichtenhofer, T. Darrell, and S. Xie, "A convnet for the 2020s," in *Proceedings of the IEEE/CVF conference on computer vision and pattern recognition*, 2022, pp. 11 976–11 986.

[43] K. He, X. Zhang, S. Ren, and J. Sun, "Deep residual learning for image recognition," in *Proceedings of the IEEE conference on computer vision and pattern recognition*, 2016, pp. 770–778.

[44] A. Dosovitskiy, L. Beyer, A. Kolesnikov, D. Weissenborn, X. Zhai, T. Unterthiner, M. Dehghani, M. Minderer, G. Heigold, S. Gelly *et al.*, "An image is worth 16x16 words: Transformers for image recognition at scale," *arXiv preprint arXiv:2010.11929*, 2020.

[45] Z. Liu, Y. Lin, Y. Cao, H. Hu, Y. Wei, Z. Zhang, S. Lin, and B. Guo, "Swin transformer: Hierarchical vision transformer using shifted windows," in *Proceedings of the IEEE/CVF international conference on computer vision*, 2021, pp. 10 012–10 022.

[46] W. Liu, D. Anguelov, D. Erhan, C. Szegedy, S. Reed, C.-Y. Fu, and A. C. Berg, "Ssd: Single shot multibox detector," in *Computer Vision–ECCV 2016: 14th European Conference, Amsterdam, The Netherlands*,

October 11–14, 2016, Proceedings, Part I 14. Springer, 2016, pp. 21–37.

[47] M. Everingham, L. Van Gool, C. K. Williams, J. Winn, and A. Zisserman, “The pascal visual object classes (voc) challenge,” *International journal of computer vision*, vol. 88, pp. 303–338, 2010.

[48] T.-Y. Lin, P. Goyal, R. Girshick, K. He, and P. Dollár, “Focal loss for dense object detection,” in *Proceedings of the IEEE international conference on computer vision*, 2017, pp. 2980–2988.

[49] M. Liang, B. Yang, S. Wang, and R. Urtasun, “Deep continuous fusion for multi-sensor 3d object detection,” in *Proceedings of the European conference on computer vision (ECCV)*, 2018, pp. 641–656.

[50] K. Shin, Y. P. Kwon, and M. Tomizuka, “Roarnet: A robust 3d object detection based on region approximation refinement,” in *2019 IEEE intelligent vehicles symposium (IV)*. IEEE, 2019, pp. 2510–2515.

[51] W. Chen, P. Li, and H. Zhao, “Ms3d: 3d object detection from monocular, stereo and point cloud for autonomous driving,” *Neurocomputing*, vol. 494, pp. 23–32, 2022.

[52] Y. Chen, S. Liu, X. Shen, and J. Jia, “Fast point r-cnn,” in *Proceedings of the IEEE/CVF international conference on computer vision*, 2019, pp. 9775–9784.

[53] A. Geiger, P. Lenz, and R. Urtasun, “Are we ready for autonomous driving? the kitti vision benchmark suite,” in *2012 IEEE conference on computer vision and pattern recognition*. IEEE, 2012, pp. 3354–3361.

[54] B. Yang, W. Luo, and R. Urtasun, “Pixor: Real-time 3d object detection from point clouds,” in *Proceedings of the IEEE conference on Computer Vision and Pattern Recognition*, 2018, pp. 7652–7660.

[55] D. P. Kingma and J. Ba, “Adam: A method for stochastic optimization,” *arXiv preprint arXiv:1412.6980*, 2014.

[56] L. N. Smith and N. Topin, “Super-convergence: Very fast training of neural networks using large learning rates,” in *Artificial intelligence and machine learning for multi-domain operations applications*, vol. 11006. SPIE, 2019, pp. 369–386.

[57] Y. Zhou, P. Sun, Y. Zhang, D. Anguelov, J. Gao, T. Ouyang, J. Guo, J. Ngiam, and V. Vasudevan, “End-to-end multi-view fusion for 3d object detection in lidar point clouds,” in *Conference on Robot Learning*. PMLR, 2020, pp. 923–932.